Materials Advances

ROYAL SOCIETY OF CHEMISTRY

PAPER

View Article Online
View Journal | View Issue

Cite this: *Mater. Adv.*, 2024, 5, 8684

A facile auto-combustion pathway for creating Mn- and Fe-doped TiO_2 nanostructures and their photocatalytic activity

Gharieb M. Meselhy, *[ab] Mostafa Y. Nassar[bc] and Sabry H. Seda[b]

Received 27th April 2024,
Accepted 24th May 2024

DOI: 10.1039/d4ma00440j

rsc.li/materials-advances

Using a combination of two fuels, an auto-combustion method was used to synthesize pure TiO_2 and doped TiO_2 with different concentrations of iron(III) (Fe) and manganese(II) (Mn) (1, 3, 5, and 7 mol%). The as-prepared materials were characterized using different techniques, including thermogravimetric analysis (TGA), X-ray diffraction (XRD), Fourier transform infrared spectroscopy (FT-IR), field emission scanning electron microscopy (FE-SEM), and high-resolution transmission electron microscopy (HR-TEM). The XRD results showed that both pure TiO_2 and all doped TiO_2 samples had the anatase phase, indicating the crystalline nature of all the as-prepared nanomaterials. Crystal violet decolorization under UV irradiation was used to assess the photocatalytic activity of the prepared samples. The findings showed that, compared to other dopant concentrations, TiO_2 with a dopant concentration of 5% Fe and 7% Mn showed the highest degradation rates (95.93% and 96.3%, respectively) at 100 and 70 min, with pseudo-first order rate constants of $k = 2.91 \times 10^{-2}$ and 4.8×10^{-2} min^{-1}, respectively. It was found that superoxide radicals and hydroxyl radicals were the main reactive species responsible for dye degradation.

1. Introduction

The mysteries and advantages of bulk materials have been unveiled *via* nanotechnology.[1] In an effort to satisfy market demands, scientists have been working feverishly to develop ideal nanomaterials ever since the nanoscale phase first emerged. The rapid growth of businesses that currently utilize a lot of water on Earth leads to water scarcity brought about by wastewater generation, and this practice puts human health, the environment, and animals in peril. The water quality required for acceptable domestic and commercial applications is negatively impacted by dyes, which are considered major pollutants. Many industries release them into the air, such as those that make textiles, paints, paper, cosmetics, medications, *etc.* Dyes tend to accumulate due to their complex chemical composition, making them more resistant to biodegradation. This might have very harmful effects, such as an increase in the demand for chemical and biological oxygen.[2–4] Due to their exceedingly bright color, variable pH, and high chemical oxygen demand, these effluents have a significant negative impact on both aquatic life systems and human health. The most prevalent effluents that the textile and printing industries release into water bodies are dyes.[5] Due to their complex aromatic structure and resistance to heat, light, and chemicals, these dyes degrade over very long periods. Therefore, it is crucial to remove these dangerous dyes from water.[6] As a result, several researchers have focused a significant portion of their work on treating wastewater from the textile industry before disposal.[7] Dyes are currently produced in large quantities and widely utilized across a variety of industries, one of which is the crystal violet dye, which is depicted in Fig. 1 as a model for application. Crystal violet (CV), also known as C.I. Basic Violet 3, is a synthetic dye commonly used in various industries, including textile, printing, and healthcare.[8] However, the release of CV into the environment can have detrimental effects due to its toxicity and carcinogenic properties.[9] Therefore, finding effective methods to degrade and remove CV from wastewater is highly important.

Different chemical, biological, and physical techniques, such as chemical oxidation,[10] reverse osmosis,[11] filtration,[12] membrane processes,[13] solvent extraction,[14] adsorption,[15] electrochemical and ultrasonication techniques, biological treatment, precipitation, and coagulation,[16] have been proposed for the removal of pollutants from wastewater. However, all these techniques have shortcomings, including post-remediation because of sludge production and the removal of adsorbents. In addition, experimental evidence has shown that dyes can be removed using biological and physical purging techniques.[17] Therefore, developing a practical way to manage water

---

[a] *The British University in Egypt, El Sherouk City, Cairo 11837, Egypt. E-mail: gharieb.meselhy@bue.edu.eg; Tel: +201226085130*
[b] *Chemistry Department, Faculty of Science, Benha University, Benha 13518, Egypt*
[c] *Chemistry Department, College of Science, King Faisal University, AL-Ahsa 31982, Saudi Arabia*

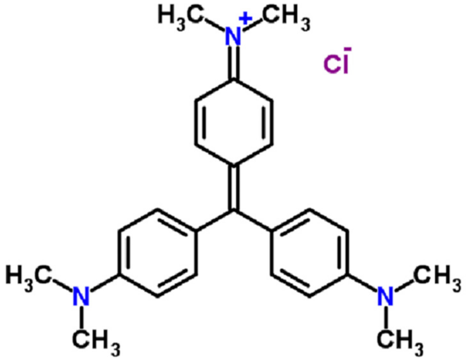

Fig. 1 Chemical structure of crystal violet as a model for photocatalytic degradation.

contamination caused by dyes has become an important and pressing problem.

Advanced oxidation processes (AOPs) have received great interest in recent years as complementary methods to conventional water treatment strategies.[18] In addition the advanced oxidation processes have an advantage over other techniques since the various radicals produced, such as superoxide radicals ($O_2^{-\bullet}$) and hydroxyl radicals ($OH^\bullet$), which are frequently utilized for photoreduction, break down the dyes into harmless chemicals.[19] Among these AOPs, heterogeneous photocatalysis has been considered the most effective and economical methodology for wastewater purification and environmental protection over the past few decades.[20] By transforming extremely dangerous pollutants into degradable molecules using light irradiation and appropriate semiconductors, photocatalysis can remove environmental toxins from the environment.[21] Numerous metal and metallic oxide-based semiconductors, including TiO_2,[22] MnO_2,[23] SnO_2,[24] Al_2O_3,[25] ZrO_2,[26] $ZnWO_4$,[27] and $Bi_2Mo_3O_{12}$,[28] have been developed with regulated band gaps to enhance charge separation and harvest visible light irradiation. Because of its non-toxicity, low cost, chemical inertness, and photochemical stability, the binary metal oxide semiconductor TiO_2 has proven to be the most suitable and appealing material.[29] Although TiO_2 has a crystalline structure that increases the number of effective and efficient active surface areas, it has several drawbacks, such as the inability to absorb light in the visible region (380 nm), a wide bandgap energy (3.2 eV), and a tendency for electron–hole recombination, which prevent its practical use.[30] Recently, several techniques have been investigated to address some of these drawbacks and hence increase the photocatalytic activity of TiO_2 for the treatment of textile effluents, including metal doping[31] (*e.g.*, iron (Fe),[32] manganese (Mn),[33] copper (Cu),[34] aluminum (Al),[35] chromium (Cr),[36] silver (Ag),[37] palladium (Pd),[38] *etc.*), non-metal doping (*e.g.*, nitrogen (N),[39] fluorine (F),[40] boron (B),[41] *etc.*) and co-doping with metals/metals (Fe–Co,[30] Fe–Pr,[42] and V–Mo[43]). There have been several documented techniques for making doped TiO_2, including hydrothermal,[44] microwave heating,[45] sol–gel,[46] precipitation,[47] and solution combustion methods.[48,49] In some studies, the photocatalytic performance of some dyes, including amaranth,[50] crystal violet,[51,52] methyl orange,[53,54] and methylene blue,[55] was examined.

Our previous study[56] on the photocatalytic efficiency of lanthanum cation-doped TiO_2 demonstrated that doping TiO_2 with La cations significantly enhances its photocatalytic efficiency, leading to effective degradation of the pollutant under UV light.

In contrast, the current work investigates the photocatalytic degradation of crystal violet dye using TiO_2 doped with manganese and iron. These alternative dopants influence the photocatalytic activity and degradation mechanism of TiO_2, as these dopants exist among the transition elements (d block) that have electronic configuration and characteristic properties different from those of La (F block). By comparing the performance and efficiency of La-doped TiO_2 with those of Mn- and Fe-doped TiO_2, we aim to identify key differences and potential improvements in photocatalytic performance. Notably, the introduction of manganese and iron may alter the electronic properties and light absorption characteristics of TiO_2, potentially leading to enhanced degradation rates and broader applicability in environmental remediation. Pure TiO_2 and doped TiO_2 with different concentrations of Mn^{2+} and Fe^{3+} are produced *via* a combustion technique. The solution combustion process offers several advantages, including cost-effectiveness, rapid synthesis and homogeneous product production.[57,58] The materials have been characterized using a variety of spectroscopic techniques and thermal investigations. The ability of the nanoparticles to remove the CV dye from the aqueous phase was investigated.

2. Materials and methods

2.1. Materials

From Advent Chembio Pvt. Ltd, India, titanium(IV) isopropoxide (TTIP) was acquired. The supplier of nitric acid (65%), citric acid, and manganese(II) acetate tetrahydrate was Lanxess India. Oxford Lab Fine Chem LLP provided the crystal violet dye, the Adwic Company supplied urea, and Qualikems Fine Chem Pvt. Ltd, India supplied iron(III) nitrate nonahydrate.

2.2. Methods

2.2.1. Synthesis of TiO_2 and (Mn, Fe)-doped TiO_2 nanoparticles. The auto-combustion approach was used to create TiO_2 nanoparticles utilizing titanium(IV) isopropoxide ($Ti(OCH(CH_3)_2)_4$) as the titania precursor and a mixture of urea and citric acid as the fuel. After 6.1 mL of titanium isopropoxide and 30 mL of distilled water were rapidly stirred for one hour, titanyl hydroxide ($TiO(OH)_2$) was produced. By combining the turbid white solution (titanyl hydroxide) with 15 mL of HNO_3, titanyl nitrate ($TiO(NO_3)_2$) was produced. After that, 2.13 g, 11.1 mmol citric acid, and 33.2 mmol urea aqueous solutions were combined with titanyl nitrate, and the mixture was agitated for 5 min. The mixture of titanyl nitrate and fuel for the combustion process is based on the presumption that the equivalence ratio C should be unity (*i.e.*, $C = (F/O) = 1$) to increase the released energy from the combustion process for each reaction, where O is the total oxidizing valence of the oxidizer (*i.e.*, titanyl nitrate) and F is the total reducing valence of the reducer (the fuel) (*i.e.*, a combination of urea and citric acid).[59] The fuel oxidizer mixture was placed on a

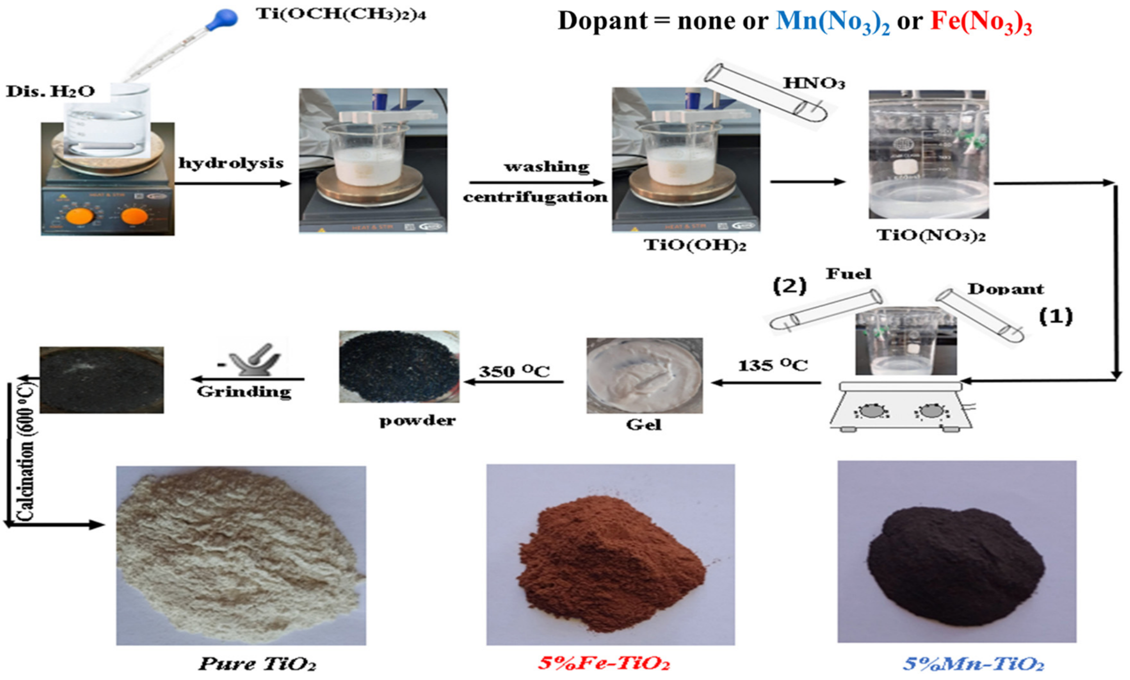

Fig. 2 Schematic proposed diagram for preparation of pure and doped TiO_2.

hot plate at 135 °C with stirring until the resin had formed, at which point it was heated at 350 °C to produce ash. To obtain pure and crystalline TiO_2 nanoparticles, the resultant ash was calcined at 650 °C for 2 h. To prepare TiO_2 doped with Mn and Fe, separately, known concentrations (1, 3, 5, and 7 mol%) of manganese(II) acetate tetrahydrate and iron(III) nitrate nonahydrate were successively added to the titanyl nitrate solution. Then, the same procedures for producing pure TiO_2 were carried out until powder (ash) was obtained. Mn–TiO_2 and Fe–TiO_2 nanoparticles were created from this ash by manually grinding it and calcining it at 600 °C for 2 h. Fig. 2 shows the proposed steps for preparing pure and doped TiO_2.

2.2.2. Preparation of Mn_2O_3 and Fe_2O_3 nanoparticles. Aqueous solutions of iron(III) nitrate nonahydrate (8.07 g) and manganese(II) nitrate were mixed with the fuel (homogeneous solutions of urea (2 g, 33.2 mmol) and citric acid (2.13 g, 11.1 mmol)). To obtain manganese(II) nitrate, an aqueous solution of manganese(II) acetate tetrahydrate (4.9 g) was treated with sodium hydroxide to adjust the pH and then treated with nitric acid. The oxidizer–reducer mixtures of manganese nitrate and iron nitrate with the fuel were heated at 135 °C to obtain a gel, which was subsequently heated to 350 °C to produce ash. The obtained powder was manually ground and calcined at 600 °C for 2 h to obtain Mn_2O_3 and Fe_2O_3 nanoparticles.

2.3. Characterization

The as-prepared samples were subjected to a range of analytical tests, including thermogravimetric analysis (TG-DTA) (SDT Q600 V20.9 Build 20), X-ray diffraction (XRD) (patterns were

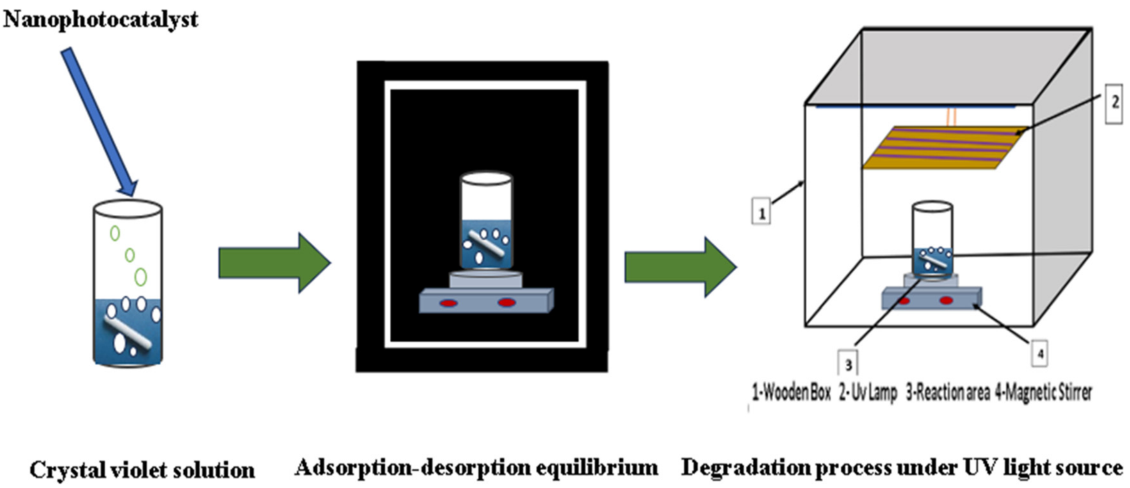

Fig. 3 The schematic shape of the experimental setup for the photocatalytic degradation reaction.

recorded on a Bruker, D8 Discover, Germany using Cu-Kα radiation (λ = 1.5406 Å), a voltage of 40 kV and a current of 40 mA with a 2 theta scanning range of 10–80♂), Fourier transform infrared (FT-IR) spectroscopy (Bomem; model MB157S) from 4000 to 400 cm^{-1} at room temperature, UV-vis spectroscopy (Jasco, model V670) to ascertain the dye concentration in the 400–700 nm range, high-resolution transmission electron microscopy (HR-TEM, JEM-2100) at an accelerating voltage of 200 kV by dispersing the samples in water on a copper grid, and field emission scanning electron microscopy (FE-SEM, JEOL JSM-6500F).

2.4. Photodegradation evaluation

Using homemade apparatus (Fig. 3) composed of a 250 mL quartz beaker, three 20-watt G13T8 UV-C mercury lamps with a maximum wavelength of 254 nm, and a multistirrer (300 rpm), the degradation of the crystal violet dye was utilized to test the photocatalytic activity of the as-prepared samples. 50 mL of crystal violet aqueous solution (20 mg L^{-1}) was mixed with different amounts of the as-prepared nanocrystalline photocatalysts (25 mg, 35 mg, 50 mg, and 75 mg). To achieve the adsorption–desorption equilibrium between the dye and the photocatalyst, the mixture was magnetically agitated for one hour before illumination. The nanophotocatalyst and dye solutions were separated by centrifuging 5 mL of the suspension at 5000 rpm for 3 min at intervals of 10 min during the photocatalytic process. Spectrophotometric detection at λ_{max} = 584 nm revealed the concentration of the dye in the supernatant.

Eqn (1) was used to estimate the degradation efficiency.

$$\text{Decolorization efficiency} = 100 \times \frac{(C_0 - C_t)}{C_0} \quad (1)$$

where C_0 is the initial concentration and C is the concentration at time t.

A series of scavenging tests were carried out to gain a thorough understanding of the active species responsible for the CV degradation process. In comparison to the initial CV concentration (50 mg of the photocatalyst and 50 mL of CV solution (20 mg L^{-1})), the scavengers were added at a 20 times molar concentration. Ascorbic acid (AA) as an $^{\bullet}O^{2-}$ scavenger,[60] EDTA–2Na as an h^+ scavenger,[61] and methyl alcohol (MA) as an $^{\bullet}OH$ scavenger[62] were independently introduced in an illustrative degradation process.

3. Results and discussion

3.1. XRD study

The XRD patterns of pure TiO_2 and doped TiO_2 with various concentrations of Fe and Mn (1, 3, 5, and 7 mol%) are shown in Fig. 4A and B, respectively, which demonstrate that both pure TiO_2 and all doped TiO_2 samples with different concentrations Fe and Mn are crystalline. According to Fig. 4A, the two most common polymorphs of TiO_2, namely, anatase (JCPDS: 01-071-1167) and rutile (JCPDS: 01-076-0318), are present in different proportions, but the anatase phase is dominant, as it constitutes 74% of the total diffraction peaks in Fe–TiO_2 and approximately 95% in Mn–TiO_2, as only one peak of 3% Mn–TiO_2(101) appears for the rutile phase. With the lattice parameters $a = b$ = 3.7892 Å, c = 9.537 Å and $\alpha = \beta = \gamma$ = 90°, all the diffraction peaks of the samples can be correlated to the anatase tetragonal TiO_2 phase. The distinctive diffraction peaks of the anatase form of pure TiO_2 are observed at 2θ = 25.39°, 37.6°, 47.9°, 53.7°, 54.9°, and 62.5°, respectively. According to the XRD pattern of Fe–TiO_2, the rutile phase is less abundant in the undoped sample, as indicated by the appearance of only two extremely weak peaks at 2θ = 27.4° (110) and 36° (101), which intensify with increasing Fe content. The reason why the anatase phase appears earlier in Fe–TiO_2 than in pure TiO_2 may be because the low charge cations (*i.e.*, <+4) can act as anatase-to-rutile transition promoters.[63]

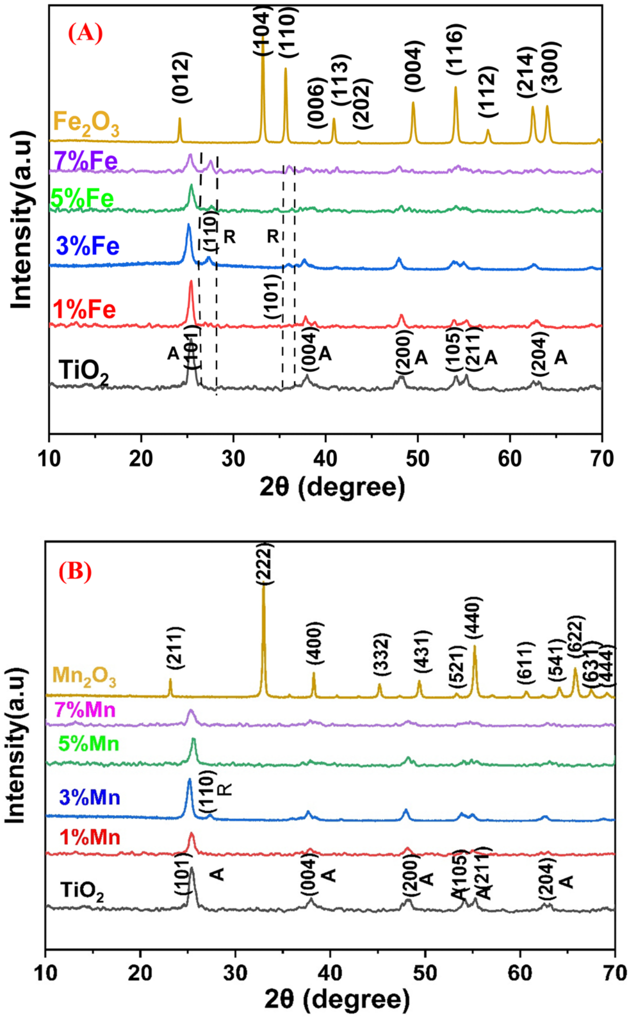

Fig. 4 XRD patterns of (A) pure oxides (TiO_2 and Fe_2O_3) and doped TiO_2 with changing concentrations (1, 3, 5, and 7 mol%) of Fe^{3+} cations and (B) pure oxides (TiO_2 and Mn_2O_3) and doped TiO_2 with different concentrations (1, 3, 5, and 7 mol%) of Mn^{2+} cations and TiO_2 pattern[56] trace previously published in reference (sm/ymri/04239411) and reproduced with permission from Taylor & Francis.

According to the calcination temperature, electronegativity, crystal structure, and atomic size that determine the substitution position, the dopant can generally act as an interstitial or substitutional impurity in the TiO_2 crystal lattice.[64] Due to the

Table 1 Crystallite sizes of pure TiO_2 and doped TiO_2

S. no.	Dopant concentration (%)	Dopant/crystallite size (nm)	Dopant/crystallite size (nm)
1	0	None/11.06	None/11.06
2	1	Mn/11.78	Fe/12.41
3	3	Mn/14.4	Fe/18.32
4	5	Mn/18.81	Fe/19.8
5	7	Mn/28.26	Fe/29.43

difference in the ionic radius between the dopant cations (Fe^{3+} and Mn^{2+}) and the host cation (Ti^{4+}), the crystallite sizes of the doped TiO_2 (Table 1) increased with increasing dopant concentration, which may be attributed to the expansion of the crystal lattice of TiO_2 resulting from the substitutional doping of the dopants. As shown in Fig. 4 and Table 2, the (101) diffraction peak of the doped TiO_2 that is displaced to a lower angle at a lower concentration shifted to a higher angle at higher concentrations, while the d value gradually increased with increasing dopant concentration and then decreased, which is consistent with Bragg's relation (eqn (1)), where d is the interplanar distance, θ is the degree of diffraction, and λ is the wavelength of the incident ray. This can be explained by the initial formation of a substitutional solid solution, which has been linked to an increase in the anatase cell volume at low dopant contents followed by a decrease in the cell volume at higher dopant contents. This expansion of the unit cell is caused by the inability of extra dopant ions to enter the TiO_2 lattice, forcing them into interstitial sites.[65] To determine the lattice parameters of the undoped and doped TiO_2 nanocrystals, the peaks corresponding to the (004) and (200) crystal planes of the anatase phase were chosen. The samples' unit cell volume and lattice parameters were determined by applying Bragg's law and eqn (2), where (hkl) are the Miller indices and a, b, and c are the lattice parameters (in a tetragonal system, $a = b \neq c$). The estimated data (Table 3) show that the estimated lattice parameters and unit cell volume of the doped TiO_2 nanoparticles differ significantly from those of the undoped sample due to the introduction of Fe^{3+} and Mn^{2+} ions into the TiO_2 lattice, which causes local distortion of the crystal structure.

Table 2 Interplanar distances and diffraction peak angle values of pure and doped TiO_2

Photocatalyst	Plane	d-spacing (Å)	Diffraction angle (θ)
TiO_2	(101)	3.4963	25.398
1% Fe–TiO_2	(101)	3.5038	25.389
3% Fe–TiO_2	(101)	3.5382	25.099
5% Fe–TiO_2	(101)	3.5059	25.38
7% Fe–TiO_2	(101)	3.5155	25.298
1% Mn–TiO_2	(101)	3.5098	25.389
3% Mn–TiO_2	(101)	3.5382	25.2
5% Mn–TiO_2	(101)	3.5081	25.57
7% Mn–TiO_2	(101)	3.5155	25.29

Table 3 Lattice parameters and cell volume of different samples estimated from XRD data

Sample	a (Å)	c (Å)	Cell volume (Å^3)
TiO_2	3.7762	9.2469	131.8638
1% Fe–TiO_2	3.7812	9.2656	132.4793
3% Fe–TiO_2	3.7900	9.3180	133.8489
5% Fe–TiO_2	3.7740	9.2008	131.0490
7% Fe–TiO_2	3.7897	9.2433	132.7543
1% Mn–TiO_2	3.7769	9.2600	132.0981
3% Mn–TiO_2	3.7899	9.3163	133.8157
5% Mn–TiO_2	3.7663	9.2581	131.3294
7% Mn–TiO_2	3.7688	9.2134	130.8716

When the doping concentration increases, the intensity of the diffraction peaks generally decreases significantly, signifying a loss of crystallinity because of lattice distortion. Strain is introduced into the system when dopant ions are added to the TiO_2 periodic crystal lattice. This causes the lattice periodicity to change and the crystal symmetry to decrease.[9] As seen from the XRD patterns, when the concentration increased, the diffraction peak width increased, indicating a systematic decrease in the grain size. The decrease in crystallinity that occurs with Fe and Mn doping can be explained by the difference in ionic charge between Ti^{4+} and the dopants (Mn^{2+} and Fe^{3+}).[66]

Eqn (4) provides the Debye–Scherrer equation, which is used to determine the average crystallite size of the photocatalysts under the as-prepared conditions. The terms "crystal size" (D), "shape factor" (k), "diffraction angle" (θ), and "full width at half-maximum height" (β) refer to the dimensions of the crystal. The results are displayed in Table 1.

$$2d\sin\theta = \lambda \tag{2}$$

$$\frac{1}{d_{hkl}{}^2} = \frac{h^2}{a^2} + \frac{k^2}{a^2} + \frac{l^2}{c^2} \tag{3}$$

$$D = \frac{(K\lambda)}{\beta\cos\theta} \tag{4}$$

The XRD pattern of the iron oxide product is depicted in Fig. 4A, and this pattern is clearly associated with the pure Fe_2O_3 phase with rhombohedral structure (space group $R\bar{3}C$ (167), lattice constants $a = 5.038$ and $c = 13.776$, JCPDS card: 01-073-3825). The Debye–Scherrer equation was used to calculate the average crystallite size of the produced Fe_2O_3 nanoparticles, which was found to be approximately 48.96 nm.

In Fig. 4B, the XRD pattern of the manganese(III) oxide product shows the cubic structure of the pure Mn_2O_3 phase (space group $Ia\bar{3}$ (206), lattice constant $a = 9.414$, and JCPDS card: 01-071-0636). The average crystallite size of the produced Mn_2O_3 nanoparticles was calculated using the Debye–Scherrer equation and was found to be approximately 45.57 nm.

3.2. Thermal analysis

According to the thermogravimetric analysis (TGA) curve on the left side of the y-axis, the weight loss of the samples is presented for the thermal assessment of pure TiO_2, 5% Mn–TiO_2, and 5% Fe–TiO_2 in Fig. 5A–C, respectively. The weight loss process consisted of three steps for all the samples. In particular, the evaporation of adsorbed water and ethanol is what predominantly contributes to the loss in the first phase,

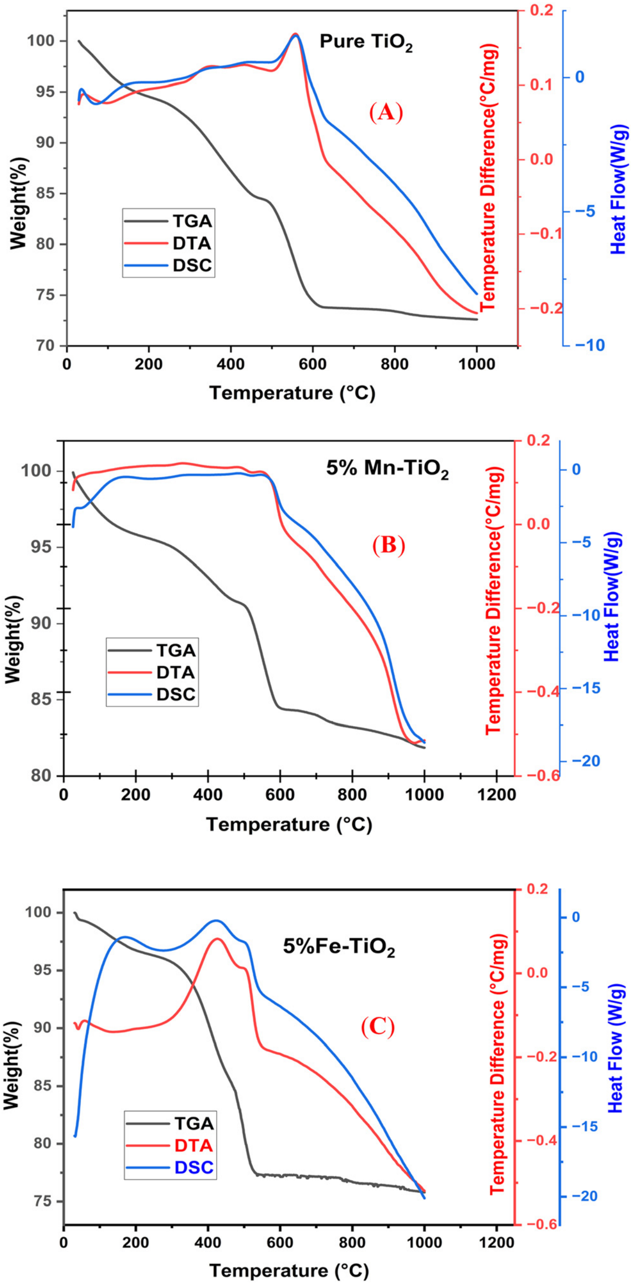

Fig. 5 TG-DTA-DSC curves of (A) pure TiO_2[56] (previously published in reference: sm/ymri/04239411 and reproduced with permission from Taylor & Francis), (B) 5% Mn–TiO_2, and (C) 5% Fe–TiO_2.

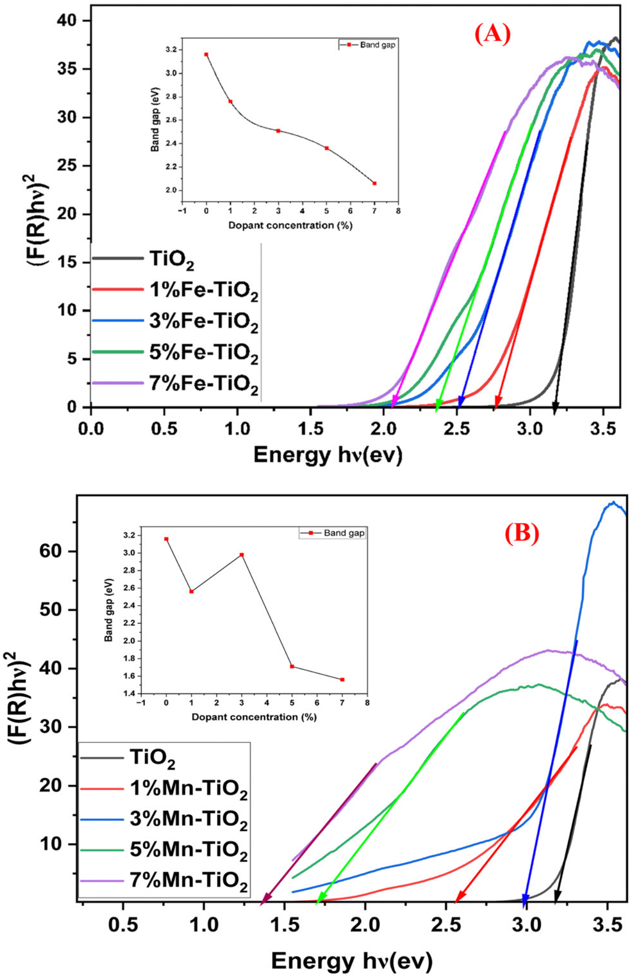

Fig. 6 Band gaps of (A) pure TiO_2 and doped-TiO_2 with different percentages (1, 3, 5, and 7 mol%) of Mn^{2+} and (B) pure TiO_2 and doped-TiO_2 with different percentages (1, 3, 5, and 7 mol%) of Fe^{3+}.

which for all samples occurs generally between 0 and 250 °C.[67] It is possible that burning organic materials at 250 °C to 500 °C will result in the second phase of weight reduction. The third stage of weight loss, which lasts between 500 °C and 700 °C, is caused by the gel's dehydroxylation.[68]

The desorption of ethanol and water is represented by a significant decrease in the peak (endothermic peak) on the differential thermal analysis (DTA) curve at approximately 100 °C for pure TiO_2 (Fig. 5A). At approximately 560 °C, heat release was predominantly caused by the decomposition of organic matter by burning. The change of TiO_2 from its amorphous phase to its crystalline anatase phase, which occurred between approximately 500 °C and 650 °C, may have contributed to the apparent decrease that occurred during this time.[69] A phase change from anatase to rutile can be observed starting at 500 °C in the exothermic peak of the pure TiO_2 DTA curve. At approximately 550 °C, the exothermic maximum appears for Mn–TiO_2. This clearly demonstrates that Mn doping hinders the phase change.[70] According to the differential scanning thermogram (DSC curve), there are two main endothermic reactions, where solvent evaporation causes the first step to begin at approximately 100 °C for all samples.[71] Due to the anatase to rutile conversion of the samples, all stages begin at nearly 620 °C.[72] Significantly, the findings of thermal analysis indicate that calcination processes performed at 650 °C and 600 °C are adequate to produce pure and doped TiO_2, respectively.

3.3. Optical activity

An important factor in the photocatalytic degradation of dyes is the band gap energy (E_g) of the nanophotocatalyst, which

Table 4 Band gap values of pure TiO_2 and TiO_2 doped with Fe and Mn

S. no.	Dopant concentration (%)	Dopant/band gap (eV)	Dopant/band gap (eV)
1	0	None/3.16	None/3.16
2	1	Mn/2.56	Fe/2.76
3	3	Mn/2.98	Fe/2.51
4	5	Mn/1.71	Fe/2.36
5	7	Mn/1.56	Fe/2.06

depends on the optical absorption coefficient and type of electronic transition of the catalyst.[73] As shown in Fig. 6A and B, the band gap of pure TiO_2 and TiO_2 doped with Fe^{3+} and Mn^{2+} at various concentrations was measured using diffuse reflection spectroscopy (DRS), and the band gap was estimated using the Kubelka–Munk technique (eqn (5)). Table 4 contains the calculated band gap values of doped and pristine TiO_2.

$$(F(R)h\nu)^{\frac{1}{n}} = A(h\nu - E_g) \tag{5}$$

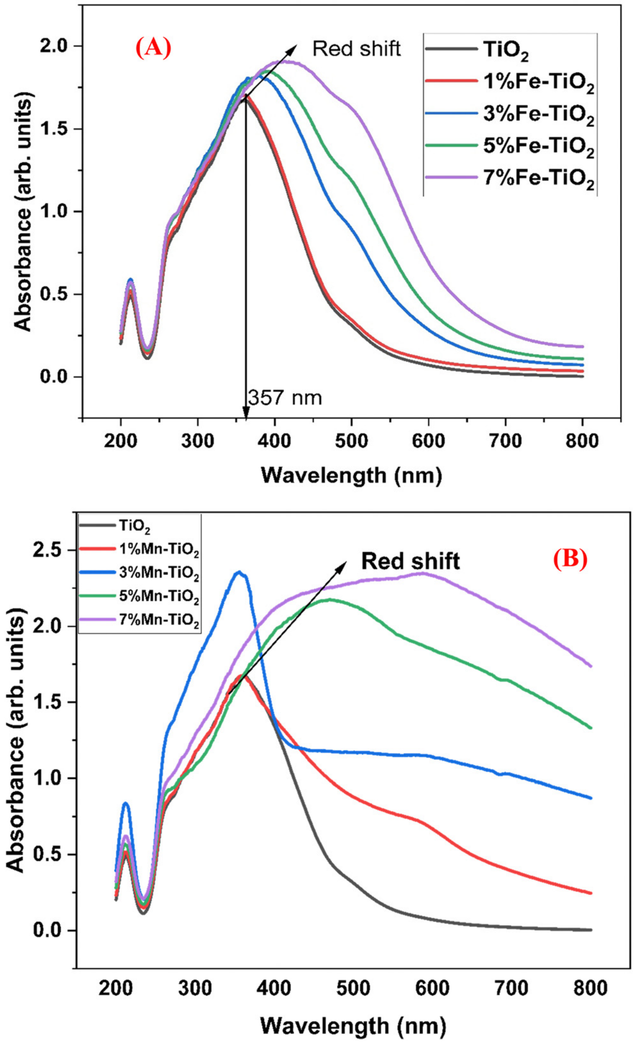

Fig. 7 Absorbance spectra of (A) pure TiO_2 and doped TiO_2 with different amounts of Fe^{3+} and (B) pure TiO_2 and doped TiO_2 with different amounts of Mn^{2+}.

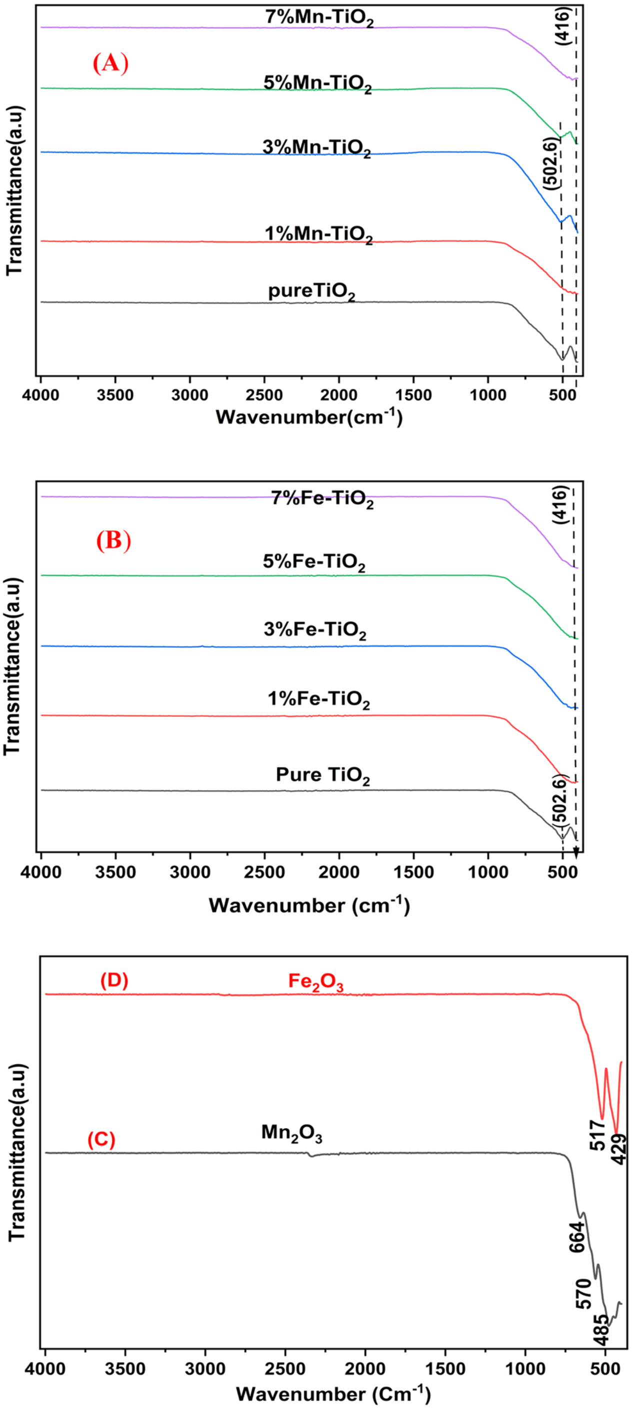

Fig. 8 FT-IR spectra of (A) pure TiO_2 and Mn–TiO_2 with varying concentrations (1, 3, 5, and 7 mol%) of Mn^{2+}, (B) pure TiO_2 and Fe-TiO_2 with varying concentrations (1, 3, 5, and 7 mol%) of Fe^{3+}, (C) Mn_2O_3 calcinated at 600 °C for 2 h, and (D) Fe_2O_3 calcinated at 600 °C for 2 h.

where $F(R)$ is the Kubelka–Munk function, A is the energy-independent constant, $h\nu$ is the input photon energy, E_g is the energy band gap, and $n = 1/2$ for a direct band gap and $n = 2$ for an indirect band gap. It is clearly observed that the band gap of doped TiO_2 was narrower than that of pure TiO_2, and the band gap of Fe–TiO_2 decreased with increasing Fe content, as shown in the inset of Fig. 6A, which is consistent with the literature.[74,75] It is possible to attribute the decreasing band gap of doped TiO_2

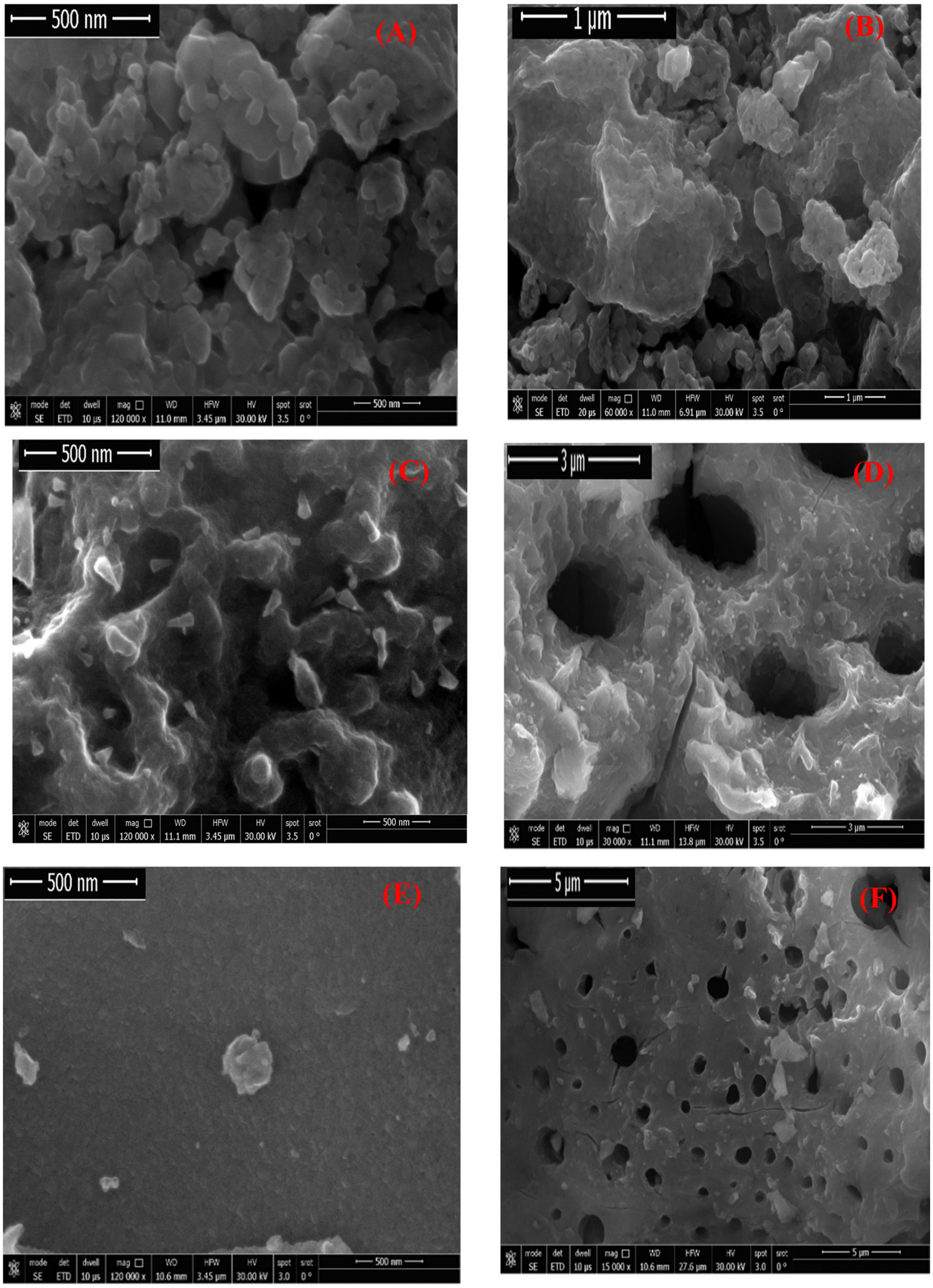

Fig. 9 FE-SEM photos of pure TiO_2 (A) and (B)[56] (previously published in reference: sm/ymri/04239411 and reproduced with permission from Taylor & Francis), calcined at 650 °C for 2 h, 7% Mn–TiO_2 (C) and (D), calcined at 600 °C for 2 h, and 5% Fe–TiO_2 (E) and (F), calcined at 600 °C for 2 h.

compared to that of pure TiO_2 to an electronic transition from the dopant's valence band (Fe^{3+}/Fe^{4+}) to the conduction band of TiO_2.[74]

Fig. 7 shows the absorbance spectra of undoped TiO_2 and TiO_2 doped with different concentrations of Fe^{3+} and Mn^{2+}. While the absorption edge of the doped TiO_2 sample is red-shifted and the light absorption is considerably enhanced in the range from 360 to 600 nm with increasing dopant concentration, the absorption edge of the undoped TiO_2 sample increases steeply at approximately 357 nm. Accordingly, the material's apparent loss in crystallinity, as verified by XRD, can be primarily responsible for the increase in absorbance that is observed with dopant concentration. The primary impact of dopant concentration is evidently a redshift of the absorption edge, which accounts for the decrease in the bandgap. The change in the electrical structure of TiO_2 as a result of Fe and Mn doping may be the cause of this redshift in the E_g.[76]

3.4. FT-IR study

The large peak below 1000 cm^{-1}, especially at 502.6 cm^{-1} in this study, was predominantly caused by Ti–O–Ti vibration,[77] as shown

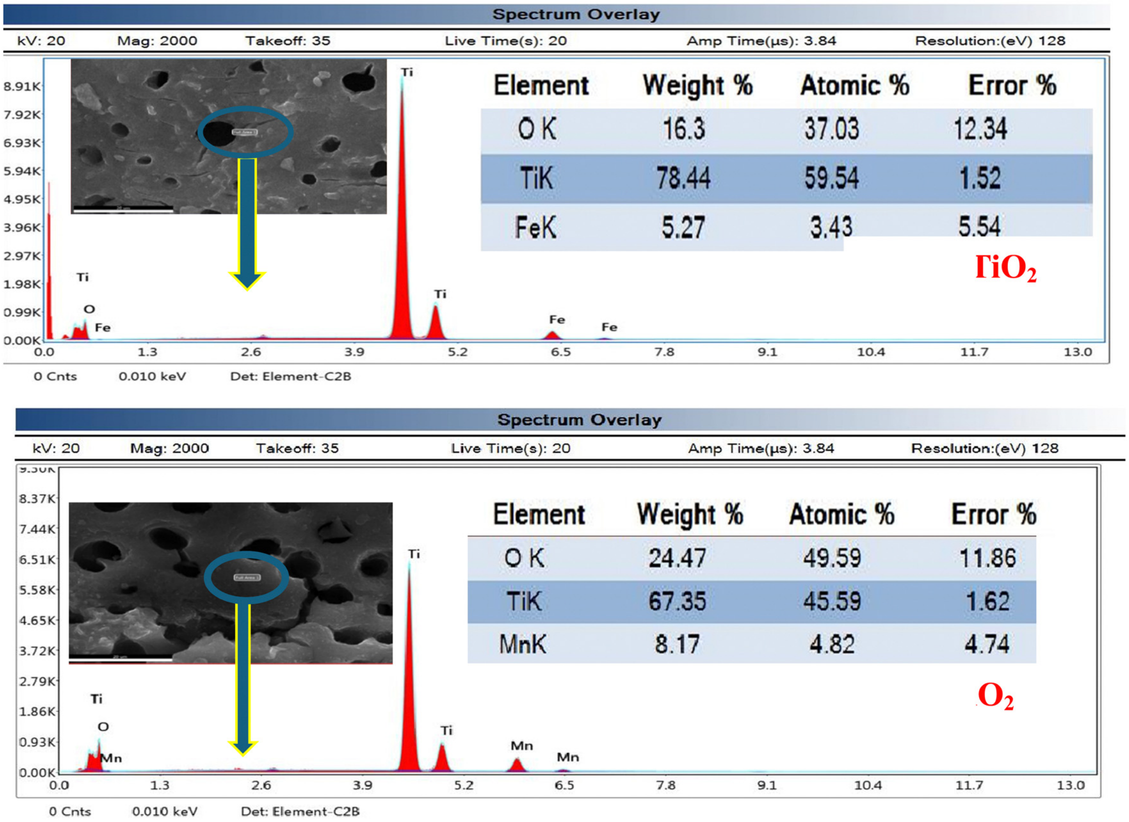

Element	Weight %	Atomic %	Error %
O K	16.3	37.03	12.34
TiK	78.44	59.54	1.52
FeK	5.27	3.43	5.54

Element	Weight %	Atomic %	Error %
O K	24.47	49.59	11.86
TiK	67.35	45.59	1.62
MnK	8.17	4.82	4.74

Fig. 10 EDX results for 5% Fe–TiO_2 and 7% Mn–TiO_2.

in Fig. 8(A and B), which shows the FTIR spectra of TiO_2 and doped TiO_2 with varying amounts of Mn and Fe. The Ti–O–Mn and Ti–O–Fe bands of the Mn–TiO_2 and Fe–TiO_2 nanoparticles may have formed as a result of the band right shift at 416 cm^{-1}. Fig. 8C shows that the Mn–O bond vibration generates three distinct peaks at approximately 485, 568, and 664 cm^{-1}, supporting the synthesis of MnO,[78] which is consistent with the XRD results. The FT-IR spectrum of Fe_2O_3 is shown in Fig. 8(D). The peaks at 429 cm^{-1} and 517 cm^{-1} are attributed to the vibration of the Fe–O bond.[79]

3.5. Morphology study

3.5.1. Field emission scanning electron microscopy (FE-SEM) and energy dispersive X-ray (EDX) results. For both pure TiO_2 and doped TiO_2 (5% Fe–TiO_2 and 7% Mn–TiO_2), FE-SEM-EDX was employed to characterize the form and distribution of the particles. Fig. 8A–F shows FE-SEM images of both pure and doped TiO_2. The images show the crystalline nature of the two varieties of TiO_2 (doped and undoped), the high interparticle adhesion, and the spherical form of the pure TiO_2 particles. The porosity of the synthesized doped products is shown in high-magnification FE-SEM images (Fig. 9D and F). Additionally, all the prepared samples had uneven shapes and were composed of aggregates of spherical and nonspherical nanoparticles.

The 5% Fe–TiO_2 and 7% Mn–TiO_2 elemental compositions were also examined *via* energy-dispersive X-ray (EDX) analysis; the results are displayed in Fig. 10. The presence of Fe–TiO_2 particles was demonstrated by the presence of Ti, Fe, and O, which were visible in the EDX spectrum of the 5% Fe–TiO_2 product. In addition, the spectrum of the 5% Mn–TiO_2 product revealed Ti, Mn, and O as supporting components in the creation of the Mn–TiO_2 particles.

3.5.2. High-resolution transmission electron microscopy (HR-TEM). TEM images match the depicted surface morphology of doped TiO_2 (7% Mn–TiO_2 and 5% Fe–TiO_2) and pure TiO_2. Fig. 11A, C, and E depicts the spherical shape of the particles and their aggregation for pure TiO_2, Fe–TiO_2, and Mn–TiO_2, respectively. The average particle sizes of pure TiO_2, 5% Fe–TiO_2, and 7% Mn–TiO_2 were approximately 64.15 nm, 23.15 nm, and 22.08 nm, respectively, as determined from the TEM images using ImageJ. Dopants can function as nucleation sites during the creation of nanoparticles, lowering the energy required for particle formation, and the increased number of nucleation sites can result in a greater number of smaller particles. This may explain why the doped TiO_2 particles were smaller than the pure TiO_2 particles. The interplanar distance (d) was calculated and found to be 0.34 nm, 0.35 nm, and 0.351 nm for TiO_2, 5% Fe–TiO_2, and 7% Mn–TiO_2, respectively, as shown in Fig. 11B, D, and F, which is consistent with the XRD data. The patterns of 5% Fe–TiO_2 and 7% Mn–TiO_2, as shown in Fig. 11G and H, respectively, were created by selected area electron diffraction and show unusually bright rings that are the result of regular and well-aligned polycrystals. The XRD results are consistent with the relative strengths of the visible

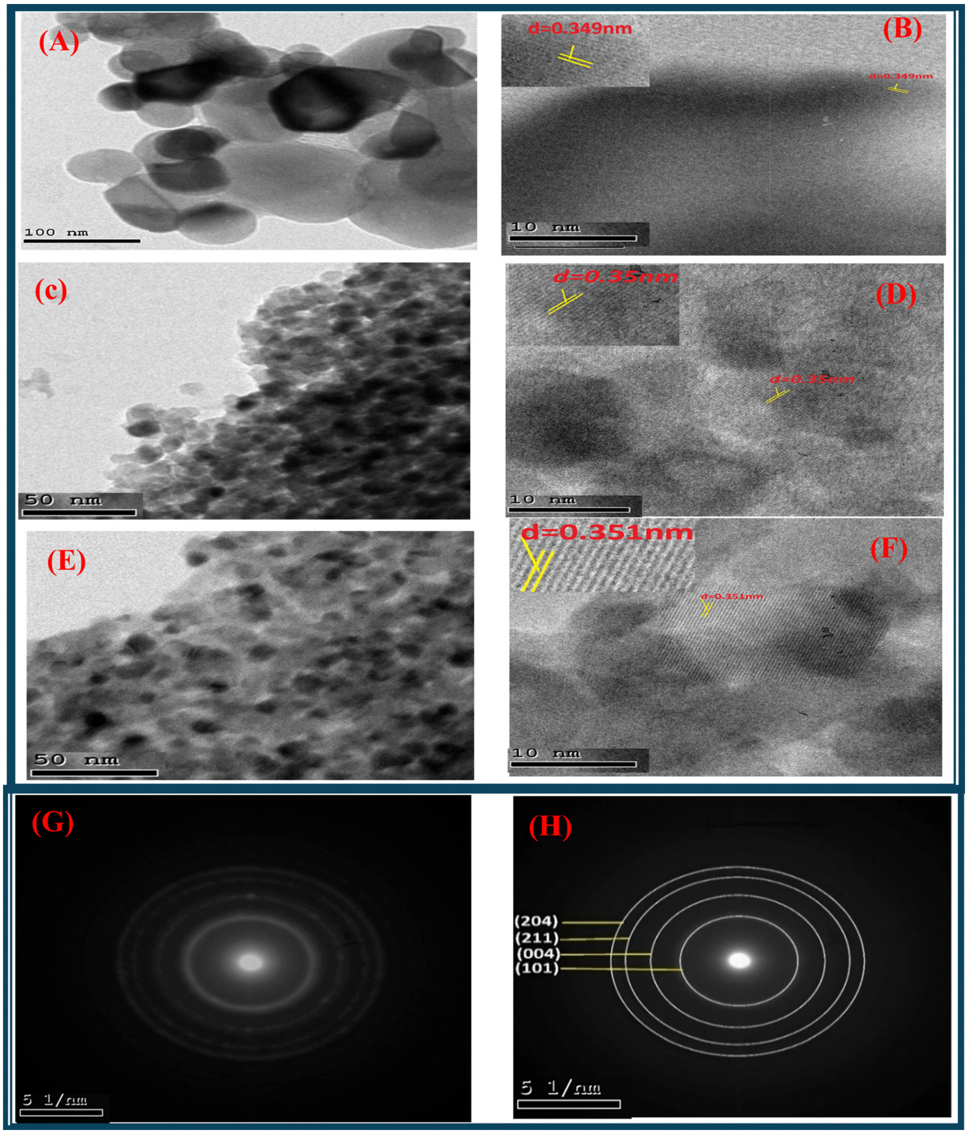

Fig. 11 HR-TEM photos of (A) and (B) pure TiO_2[56] (previously published in reference: sm/ymri/04239411, and reproduced with permission from Taylor & Francis), (C) and (D) 5% Fe–TiO_2, (E) and (F) 7% Mn–TiO_2 and (G) and (H) SAED patterns of 5% Fe–TiO_2 and 7% Mn–TiO_2, respectively.

diffraction rings, which may be indexed to the (101), (004), (211), and (204) planes.

3.6. Photocatalytic assessment

To compare the results, photocatalytic evaluation of TiO_2, Fe_2O_3, and Mn_2O_3 and doped TiO_2 with different cations of Fe^{3+} and Mn^{2+} at various concentrations ranging from 1 to 7 mol% was carried out. A total of 20 ppm (20 mg L^{-1}) crystal violet aqueous solution was mixed with 50 mg of the as-prepared catalyst. As illustrated in Fig. 12A and B, the photocatalytic performance of the as-prepared samples Fe–TiO_2 and Mn–TiO_2 was investigated at 120 and 100 min, respectively. Further research on the kinetics of the photocatalytic degradation of CV was conducted. The plot of $\ln(C_t/C_0)$ *vs.* irradiation time intervals clearly demonstrates a linear relationship, where C_0 is the dye concentration prior to irradiation and after attaining adsorption/desorption equilibrium and C_t is the actual dye concentration at irradiation time t. For the Fe–TiO_2 and Mn–TiO_2 samples, respectively, Fig. 12C and D show linear correlations between curves that follow the equation $\ln(C_t/C_0) = Kt$, where K is the first-order rate constant. It is common to observe strong correlations, which prove that the reaction kinetics follow a pseudo-first-order rate law. The first-order constants are shown in Table 5.

3.6.1. Effect of dopant concentration. To examine the photocatalytic performance of pure TiO_2 and doped TiO_2 with various concentrations of Fe and Mn ranging from 1 to 7 mol%, the degradation of the CV dye in an aqueous suspension solution under UV light in the presence of ambient oxygen was examined. Fig. 13A and B illustrates the rate of decolorization of CV in the presence of pure TiO_2 and Fe and Mn-doped TiO_2 (dopant concentration ranging from 1 to 7 mol%). The figure demonstrates that doped TiO_2 with different Fe and Mn dopant concentrations was more effective than pure TiO_2, and

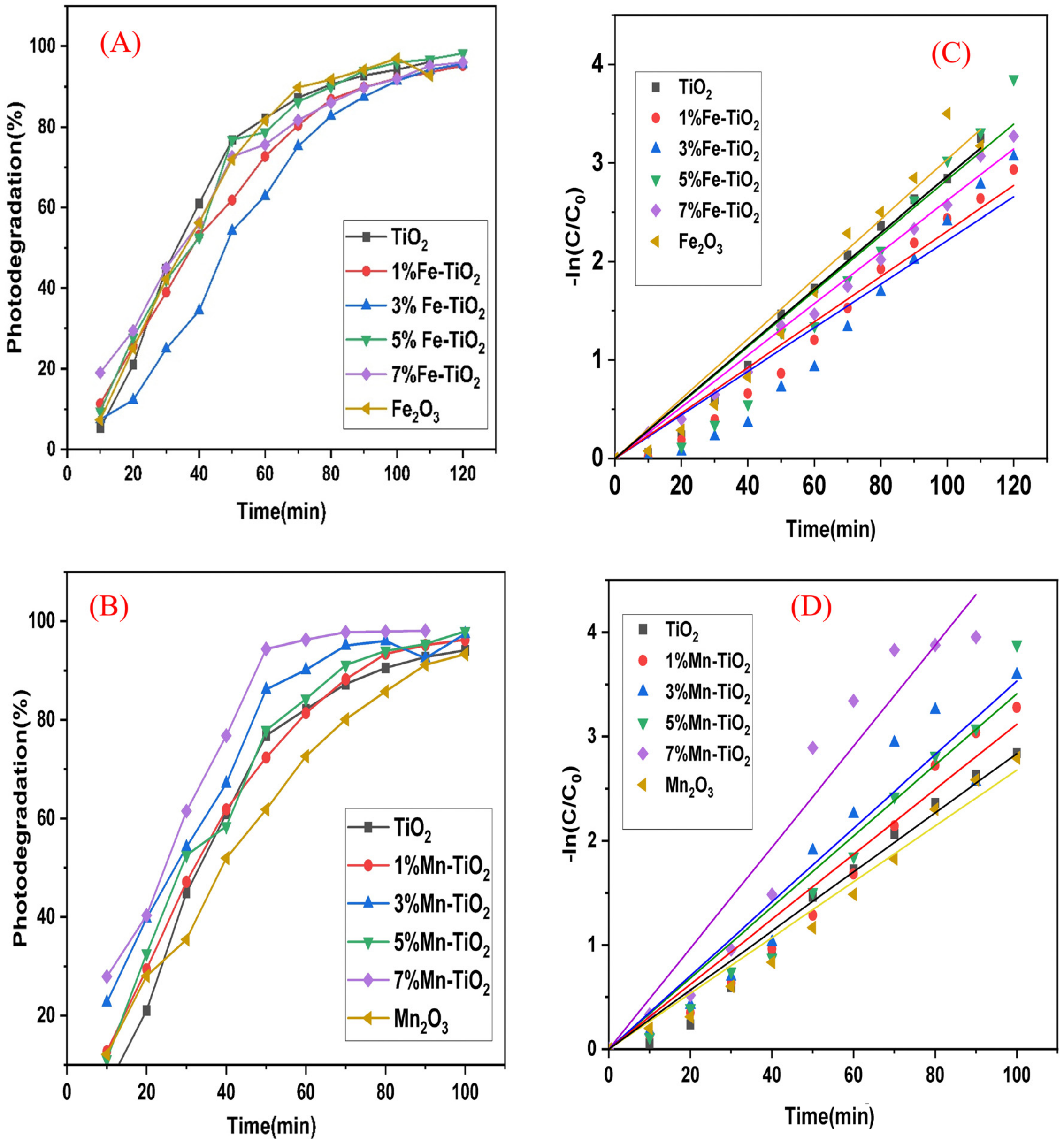

Fig. 12 Effect of contact time on the degradation rate of an aqueous solution of CV in the presence of (A) pure oxides (TiO_2 and Fe_2O_3) and Fe–TiO_2, (B) pure oxides (TiO_2 and Mn_2O_3) and Mn–TiO_2. Corresponding pseudo-first-order kinetic fits for the photocatalytic degradation reaction of CV using (C) pure oxides (TiO_2 and Fe_2O_3) and Fe–TiO_2 and (D) pure oxides (TiO_2 and Mn_2O_3) and Mn–TiO_2 under UV light and with the change in concentration in relation to time (min) upon irradiation of an aqueous solution of CV in the presence of (B) TiO_2, Fe_2O_3 and Fe–TiO_2 and (D) pure TiO_2, Mn_2O_3, and Mn–TiO_2 under UV light.

Table 5 Calculated kinetic parameters for the degradation processes

S. no.	Dopant concentration	Parameters/Mn–TiO_2		Parameters/Fe–TiO_2	
		R^2	K (min^{-1})	R^2	K (min^{-1})
1	0	0.992	2.89×10^{-2}	0.992	2.89×10^{-2}
2	1	0.984	3.1×10^{-2}	0.985	2.31×10^{-2}
3	3	0.972	3.5×10^{-2}	0.956	2.21×10^{-2}
4	5	0.981	3.4×10^{-2}	0.971	2.91×10^{-2}
5	7	0.976	4.8×10^{-2}	0.996	2.61×10^{-2}
6	Simple oxides	Mn_2O_3		Fe_2O_3	
		0.989	2.6×10^{-2}	0.981	3.03×10^{-2}

it also demonstrates that 5% Fe–TiO_2 and 7% Mn–TiO_2 achieved the highest degradation of CV in comparison to other dopant concentrations and that the optimal time for degradation was 100 and 70 min, achieving 95.93% and 97%, respectively. Table 6 contrasts the primary degradation results with those of a few similar materials, highlighting their salient features and working conditions.

3.6.2. Effect of photocatalyst amount. Furthermore, the effectiveness of the photocatalytic degradation of different pollutants is similarly influenced by the amount of photocatalyst. It directly determines how easily contaminants can

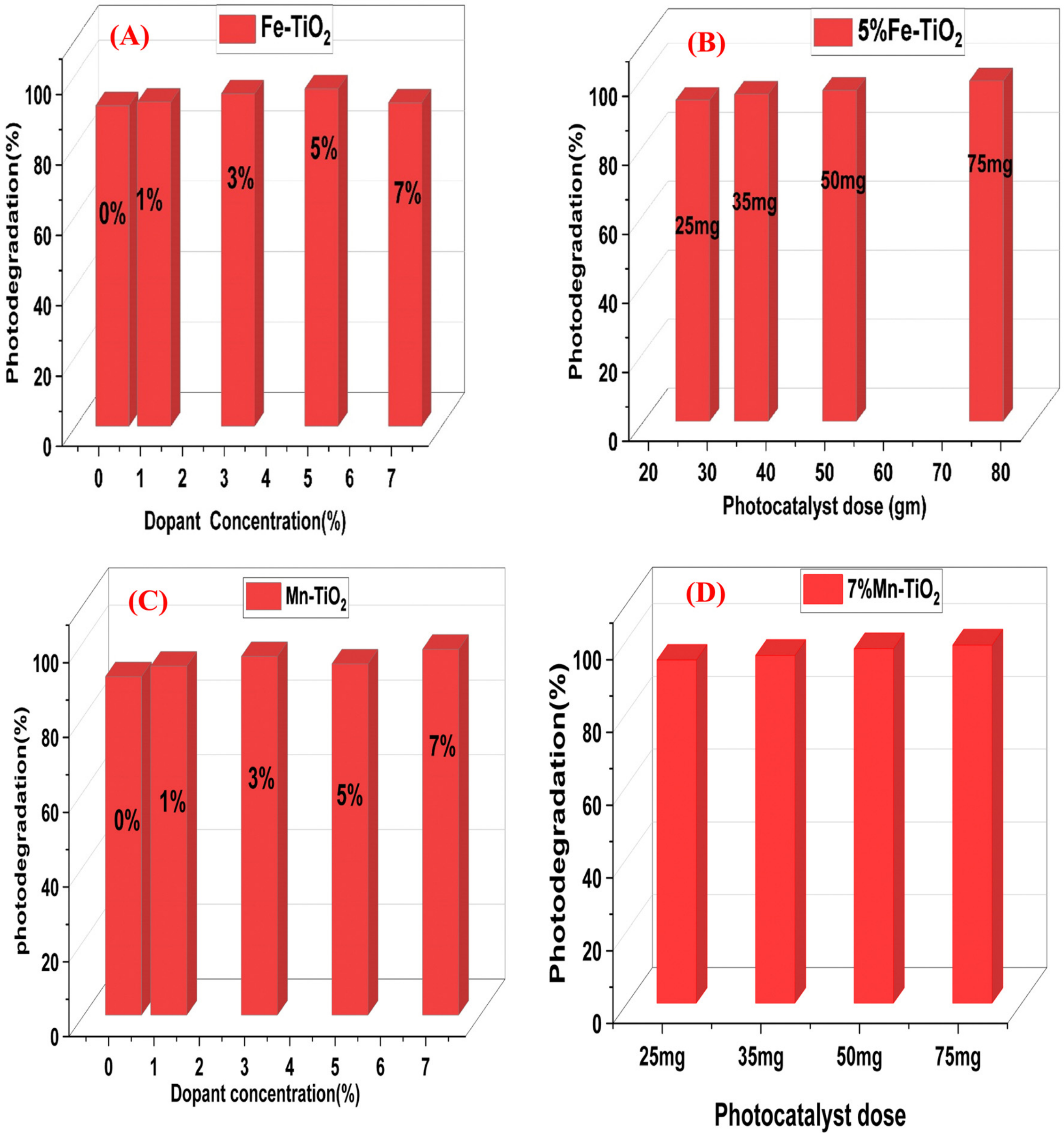

Fig. 13 Photocatalytic assessment of (A) Fe-doped TiO_2 (at different Fe concentrations), (B) Mn-doped TiO_2 (at different Mn concentrations), (C) 5% Fe-doped TiO_2 (at different concentrations) and (D) 7% Mn–TiO_2 (at different concentrations) for the decolorization of CV.

become entrapped at surface-active sites, thus influencing color removal efficiency.[84] The photocatalytic activity of 5% Fe–TiO_2 and 7% Mn–TiO_2 (changing the amount from 25 mg to 75 mg), the most efficient catalyst concentrations among the other Fe and Mn concentrations, was tested for the degradation of CV, as shown in Fig. 13(C and D). 75 mg of the catalyst showed the maximum degradation compared to the other concentrations of 5% Fe–TiO_2 and Mn–TiO_2 (98.67% and 97.78% at 100 and 70 min, respectively). As shown in the figure, the degradation efficiency increased with increasing photocatalyst amount from 25 mg to 75 mg. This increase in the rate of degradation can be attributed to the higher amount of the photocatalyst, which produced a larger surface area and more active sites, improving the trapping of CV molecules.[8]

3.6.3. Effect of active species scavenging. Superoxide radicals ($^{\bullet}O_2^-$), positive holes (h^+), and hydroxyl radicals ($^{\bullet}OH$) were the active species whose roles were identified by observing changes in the photocatalytic degradation of CV following the addition of scavengers to the photocatalytic system. The variation in CV degradation before and after the scavengers were added to the photocatalytic system is depicted in Fig. 14. The degradation efficiency of CV with (3% La–TiO_2, 5% Fe–TiO_2, and 7% Mn–TiO_2) was nearly the same with and without the addition of EDTA-2Na, which suggests that positive holes (h^+) are not involved in the degradation of CV. When MA and AA were added, the degradation of CV decreased sharply, and the MA decreased from 92.5%, 82%, and 94.42% to 62%, 65%, and 65% in the presence of 3% La–TiO_2, 5% Fe–TiO_2, and 7%

Table 6 Comparison of the photodegradation capabilities Fe–TiO_2 and Mn–TiO_2 for CV with those of several similar photocatalysts

Photocatalyst	Preparation method	Degradation (%)	Optimum conditions	Ref.
Fe–TiO_2 and Mn–TiO_2	Solution combustion	95.9 and 96.3	The initial concentration of CV dye is 20 mg L^{-1}, the photocatalyst amount is 50 mg, T = 298 K, the contact time is 100 and 70 min and UV light is the light source	This work
Au-reduced graphene oxide nanocomposite	Repurposing electronic waste and dry batteries	99%	The initial concentration of CV dye is 10 mg L^{-1}, pH = 10, the photocatalyst amount is 40 mg, T = 298 K, the contact time is 30 min and visible light is the light source	8
La-doped TiO_2	Solution combustion	95.98	The initial concentration of CV dye is 20 mg L^{-1}, the photocatalyst amount is 50 mg, T = 298 K, the contact time is 70 min and UV light is the light source	56
Fe-doped TiO_2	Reverse-micelle sol–gel	96	The initial concentration of CV dye is 10 mg L^{-1}, with 3 g L^{-1} photocatalyst amount, the contact time is 180 min and visible light is the light source	65
In_2O_3 nanocapsules	Biogenic reflux method	90	The initial concentration of CV dye is 10 mg L^{-1}, with 0.1 g L^{-1} photocatalyst amount, the contact time is 180 min and visible light is the light source	80
Ag-doped TiO_2	Hydrothermal method	99	The initial concentration of CV dye is 20 mg L^{-1}, with 1 g L^{-1} photocatalyst amount, the contact time is 105 min and UV light is the light source	81
p–n NiO–ZnO	Homogeneous precipitation method	100	The initial concentration of CV dye is 100 mg L^{-1}, pH = 11, the photocatalyst amount is 0.1 g/50 mL, T = 298 K, the contact time is 180 min and UV light is the light source	82
$ZnFe_2O_4$ nanoparticles	The co-precipitation oxidation method	96	The initial concentration of CV dye is 10 ppm, pH = 7, the photocatalyst amount is 30 mg, T = 298 K, the contact time is 30 min and sun light is the light source	83

Mn–TiO_2, respectively, in just 55 minutes. In terms of AA, the percentages decreased from 92.5%, 82%, and 94.42% to 53%, 55%, and 58%, respectively. Based on these findings, we may conclude that the primary active species throughout the photocatalytic process were hydroxyl radicals (${}^{\bullet}OH$) and superoxide radicals (${}^{\bullet}O_2{}^{-}$).

3.6.4. Photocatalytic degradation mechanism. Crystal violet molecules can undergo direct or indirect photodegradation on the surface of doped TiO_2. In direct photodegradation, crystal violet molecules directly interact with the photocatalyst surface and undergo oxidation reactions. Indirect photodegradation involves the reaction between crystal violet and reactive oxygen species (ROS) generated by a photocatalyst. During these reactions, the chromophoric groups of crystal violet, which are responsible for its color, are broken down into smaller, less colored fragments. Eventually, these fragments can mineralize into harmless inorganic compounds such as carbon dioxide, water, and inorganic ions.[85]

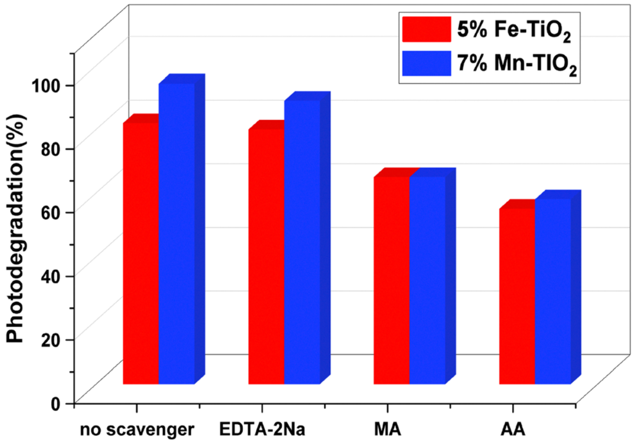

Fig. 14 Photocatalytic degradation of CV using 5% Fe–TiO_2 and 7% Mn–TiO_2 under UV light irradiation in the presence of various scavengers.

According to the photocatalytic degradation mechanism (eqn (6)–(13)), the photocatalytic degradation of CV using pure TiO_2 or doped TiO_2 involves the generation of reactive oxygen species (ROS) upon exposure to UV light. The ROS, such as hydroxyl radicals (${}^{\bullet}OH$), superoxide radicals (${}^{\bullet}O^{2-}$), and holes (h^+), can oxidize and breakdown CV molecules into smaller, less harmful compounds, which speeds up the fading of color. Reactive oxygen species, such as hydroxyl radicals (${}^{\bullet}OH$) and superoxide radicals (${}^{\bullet}O^{2-}$), form as a result of the reaction of holes with hydroxide ions and the reaction of electrons with dissolved oxygen, respectively.[86] Fig. 15, which presents the suggested mechanism, illustrates this phenomenon. The process follows a pseudo-first-order rate law, where the degradation rate depends on the concentration of CV, catalyst amount, and light intensity.

$$\text{Dopant–TiO}_2 + h\nu \rightarrow (e_{cb}{}^{-} + h_{vb}{}^{+})@\text{dopant–TiO}_2 \quad (6)$$

$$H_2O + h_{vb}{}^{+} \rightarrow OH^{\bullet} + H^{+} \quad (7)$$

$$O_2 + e_{cb}{}^{-} \rightarrow O_2{}^{-\bullet} \quad (8)$$

$$O_2{}^{-\bullet} + H^{+} \rightarrow HOO^{\bullet} \quad (9)$$

$$2HOO^{\bullet} \rightarrow H_2O_2 + O_2 \quad (10)$$

$$H_2O_2 \rightarrow 2OH^{\bullet} \quad (11)$$

$$CV + OH^{\bullet} \rightarrow \text{degraded products} \quad (12)$$

$$CV + O_2{}^{-\bullet} \rightarrow \text{degraded products} \quad (13)$$

4. Conclusion

Both pure TiO_2 and doped TiO_2 with various amounts of Fe and Mn exhibited crystallinity, according to the XRD study, and the

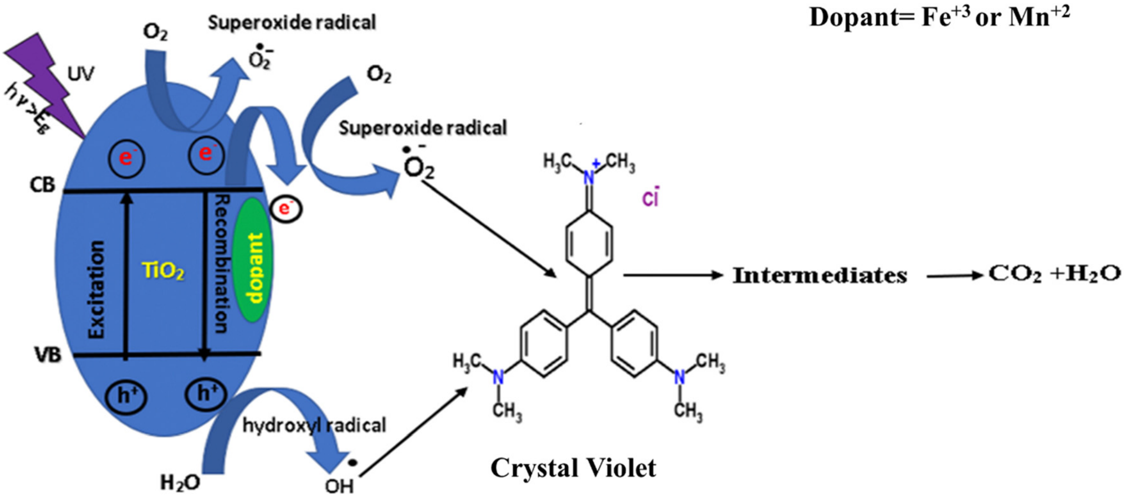

Fig. 15 Proposed mechanism of TiO_2 with dopants for the photocatalytic decolorization of CV.

peaks of the anatase phase were dominant. In comparison to those of TiO_2, Fe_2O_3, and Mn_2O_3, the photocatalytic activity of TiO_2 with Fe and Mn dopant concentrations of 1%, 3%, 5%, and 7% was high. Compared to other dopant concentrations, TiO_2 with dopant concentrations of 5% Fe and 7% Mn demonstrated the highest photocatalytic activity for the decolorization of the crystal violet dye. By increasing the amount from 25 mg to 75 mg, the photocatalytic efficiency of 5% Fe–TiO_2 and 7% Mn–TiO_2 increased, and an amount of 75 mg for both materials exhibited maximum degradation compared to the other amounts. With $K = 2.91 \times 10^{-2}$ and 4.8×10^{-2} min^{-1}, 5% Fe–TiO_2 and 7% Mn–TiO_2 exhibited the highest rate constants of the reaction in comparison to the other dopant concentrations. It was found that superoxide and hydroxyl radicals were the primary active species during the photocatalytic process.

Note after first publication

Following the initial publication, a reader's comments led to revisions in the topological study. The authors had examined the topology, including Fig. 1 and 3, but it was decided to alter these figures after speaking with an expert. This version of the text reports an accurate analysis, and it also includes modified captions for Fig. 4, 5, 9 and 11. This new analysis is also reflected in the manuscript introduction and highlights the novelty of this topology.

Data availability

The datasets used and analyzed during the current study are available from the corresponding author upon reasonable request.

Conflicts of interest

There are no conflicts of interest to declare.

Acknowledgements

The corresponding author, "Gharieb M. Meselhy," expresses his sincere gratitude to his spouse, "Shereen El Sheikh," for her unwavering support.

References

1 M. Y. Nassar, M. S. NourEldien, I. M. Ibrahim and H. M. Aly, A Facile Hydrothermal Synthesis of S-VO_2-Cellulose Nanocomposite for Photocatalytic Degradation of Methylene Blue Dye, *Processes*, 2023, **11**(5), 1322.
2 H. Liyanaarachchi, C. Thambiliyagodage, H. Lokuge and S. Vigneswaran, Kinetics and Thermodynamics Study of Methylene Blue Adsorption to Sucrose- and Urea-Derived Nitrogen-Enriched, Hierarchically Porous Carbon Activated by KOH and H_3PO_4, *ACS Omega*, 2023, **8**(18), 16158–16173, DOI: 10.1021/acsomega.3c00339.
3 C. P. Liyanage and K. Yamada, Impact of population growth on the water quality of natural water bodies, *Sustainability*, 2017, **9**(8), 1405.
4 D. Chahar, D. Kumar, P. Thakur and A. Thakur, Visible light induced photocatalytic degradation of methylene blue dye by using Mg doped Co–Zn nanoferrites, *Mater. Res. Bull.*, 2023, **162**, 112205, DOI: 10.1016/j.materresbull.2023.112205.
5 N. Ali, A. Zada and M. Zahid, *et al.*, Enhanced photodegradation of methylene blue with alkaline and transition-metal ferrite nanophotocatalysts under direct sun light irradiation, *J. Chinese Chem. Soc.*, 2019, **66**(4), 402–408.
6 R. Beura, R. Pachaiappan and T. Paramasivam, Photocatalytic degradation studies of organic dyes over novel Ag-loaded ZnO-graphene hybrid nanocomposites, *J. Phys. Chem. Solids*, 2021, **148**, 109689, DOI: 10.1016/j.jpcs.2020.109689.
7 P. Heidari and S. M. Masoudpanah, Structural, magnetic and optical properties and photocatalytic activity of magnesium-calcium ferrite powders, *J. Phys. Chem. Solids*, 2021, **148**, 109681.

8 S. H. Al-Ansari, H. Gomaa, R. D. Abdel-Rahim, G. A. M. Ali and A. M. Nagiub, Recycled gold-reduced graphene oxide nanocomposite for efficient adsorption and photocatalytic degradation of crystal violet, *Sci. Rep.*, 2024, **14**(1), 1–16, DOI: **10.1038/s41598-024-54580-1**.

9 Z. Yan, H. Yang and H. Dong, *et al.*, Occurrence and ecological risk assessment of organic micropollutants in the lower reaches of the Yangtze River, China: A case study of water diversion, *Environ. Pollut.*, 2018, **239**, 223–232.

10 W. H. Glaze, J. W. Kang and D. H. Chapin, The chemistry of water treatment processes involving ozone, hydrogen peroxide and ultraviolet radiation, *Ozone: Sci. Eng.*, 1987, **9**(4), 335–352.

11 L. F. Greenlee, D. F. Lawler, B. D. Freeman, B. Marrot and P. Moulin, Reverse osmosis desalination: water sources, technology, and today's challenges, *Water Res.*, 2009, **43**(9), 2317–2348.

12 M. W. Jornitz, *Filtration and Purification in the Biopharmaceutical Industry*, CRC Press, 2019.

13 C. Thamaraiselvan and M. Noel, Membrane processes for dye wastewater treatment: recent progress in fouling control, *Crit. Rev. Environ. Sci. Technol.*, 2015, **45**(10), 1007–1040.

14 D. T. Santos, C. L. C. Albuquerque and M. A. A. Meireles, Antioxidant dye and pigment extraction using a homemade pressurized solvent extraction system, *Procedia Food Sci.*, 2011, **1**, 1581–1588.

15 P. Mondal, C. B. Majumder and B. Mohanty, Laboratory based approaches for arsenic remediation from contaminated water: recent developments, *J. Hazard. Mater.*, 2006, **137**(1), 464–479.

16 R. Al-Tohamy, S. S. Ali and F. Li, *et al.*, A critical review on the treatment of dye-containing wastewater: Ecotoxicological and health concerns of textile dyes and possible remediation approaches for environmental safety, *Ecotoxicol. Environ. Saf.*, 2022, **231**, 113160.

17 G. Mustafa, M. K. Aziz and L. Sharma, *et al.*, Synthesis and characterization of biocone-like ZNO nanoparticles as antibacterial agent and as photocatalyst for removal of hazardous methyl orange dye, *J. Pharm. Negat. Results*, 2023, **12**, 5480–5490.

18 A. Habibi-Yangjeh, S. Asadzadeh-Khaneghah, S. Feizpoor and A. Rouhi, Review on heterogeneous photocatalytic disinfection of waterborne, airborne, and foodborne viruses: can we win against pathogenic viruses?, *J. Colloid Interface Sci.*, 2020, **580**, 503–514.

19 C. Thambiliyagodage, A. Kumara, M. Jayanetti, L. Usgodaarachchi, H. Liyanaarachchi and B. Lansakara, Fabrication of dual Z-scheme g-C_3N_4/Fe_2TiO_5/Fe_2O_3 ternary nanocomposite using natural ilmenite for efficient photocatalysis and photosterilization under visible light, *Appl. Surf. Sci. Adv.*, 2022, **12**, 100337, DOI: **10.1016/j.apsadv.2022.100337**.

20 R. Mohammed, M. E. M. Ali, E. Gomaa and M. Mohsen, Promising MoS_2–ZnO hybrid nanocomposite photocatalyst for antibiotics, and dyes remediation in wastewater applications, *Environ. Nanotechnol., Monit. Manage.*, 2023, **19**, 100772.

21 H. M. Yates, M. G. Nolan, D. W. Sheel and M. E. Pemble, The role of nitrogen doping on the development of visible light-induced photocatalytic activity in thin TiO_2 films grown on glass by chemical vapour deposition, *J. Photochem. Photobiol., A*, 2006, **179**(1–2), 213–223.

22 D. Chen, Y. Cheng and N. Zhou, *et al.*, Photocatalytic degradation of organic pollutants using TiO_2-based photocatalysts: A review, *J. Cleaner Prod.*, 2020, **268**, 121725.

23 X. Bao, Z. Qin, T. Zhou and J. Deng, In-situ generation of gold nanoparticles on MnO_2 nanosheets for the enhanced oxidative degradation of basic dye (Methylene Blue), *J. Environ. Sci.*, 2018, **65**, 236–245.

24 M. Najjar, H. A. Hosseini and A. Masoudi, *et al.*, Green chemical approach for the synthesis of SnO_2 nanoparticles and its application in photocatalytic degradation of Eriochrome Black T dye, *Optik*, 2021, **242**, 167152.

25 S. Anbarasu, S. Ilangovan and K. Usharani, *et al.*, Visible light mediated photocatalytic activity of Ni-doped Al_2O_3 nanoparticles, *Surf. Interfaces*, 2020, **18**, 100416.

26 A. Alagarsamy, S. Chandrasekaran and A. Manikandan, Green synthesis and characterization studies of biogenic zirconium oxide (ZrO_2) nanoparticles for adsorptive removal of methylene blue dye, *J. Mol. Struct.*, 2022, **1247**, 131275.

27 G. V. Geetha, S. P. Keerthana, K. Madhuri and R. Sivakumar, Effect of solvent volume on the properties of $ZnWO_4$ nanoparticles and their photocatalytic activity for the degradation of cationic dye, *Inorg. Chem. Commun.*, 2021, **132**, 108810.

28 M. Kristl, N. Sinanović, S. Gyergyek and J. Kristl, Sonochemical synthesis, characterization and photocatalytic activity of $Bi_2Mo_3O_{12}$, *Inorg. Chem. Commun.*, 2020, **112**, 107699.

29 M. R. Al-Mamun, S. Kader, M. S. Islam and M. Z. H. Khan, Photocatalytic activity improvement and application of UV-TiO_2 photocatalysis in textile wastewater treatment: A review, *J. Environ. Chem. Eng.*, 2019, **7**(5), 103248.

30 A. El Mragui, Y. Logvina, L. Pinto da Silva, O. Zegaoui and J. C. G. Esteves da Silva, Synthesis of Fe-and Co-doped TiO_2 with improved photocatalytic activity under visible irradiation toward carbamazepine degradation, *Materials*, 2019, **12**(23), 3874.

31 J. Choi, H. Park and M. R. Hoffmann, Effects of single metal-ion doping on the visible-light photoreactivity of TiO_2, *J. Phys. Chem. C*, 2010, **114**(2), 783–792.

32 H. Wang, N. Zhang and G. Cheng, *et al.*, Preparing a photocatalytic Fe doped TiO_2/rGO for enhanced bisphenol A and its analogues degradation in water sample, *Appl. Surf. Sci.*, 2020, **505**, 144640.

33 A. J. Moreira, J. O. D. Malafatti and T. R. Giraldi, *et al.*, Prozac® photodegradation mediated by Mn-doped TiO_2 nanoparticles: evaluation of by-products and mechanisms proposal, *J. Environ. Chem. Eng.*, 2020, **8**(6), 104543.

34 S. Ahadi, N. S. Moalej and S. Sheibani, Characteristics and photocatalytic behavior of Fe and Cu doped TiO_2 prepared by combined sol–gel and mechanical alloying, *Solid State Sci.*, 2019, **96**, 105975.

35 R. Kaushik, P. K. Samal and A. Halder, Degradation of fluoroquinolone-based pollutants and bacterial inactivation by visible-light-active aluminum-doped TiO_2 nanoflakes, *ACS Appl. Nano Mater.*, 2019, **2**(12), 7898–7909.

36 T. Umebayashi, T. Yamaki, T. Sumita, S. Yamamoto, S. Tanaka and K. Asai, UV-ray photoelectron and ab initio band calculation

studies on electronic structures of Cr- or Nb-ion implanted titanium dioxide, *Nucl. Instrum. Methods Phys. Res., Sect. B*, 2003, **206**, 264–267, DOI: **10.1016/S0168-583X(03)00740-7**.

37 J. Yang and X. Luo, Ag-doped TiO_2 immobilized cellulose-derived carbon beads: One-Pot preparation, photocatalytic degradation performance and mechanism of ceftriaxone sodium, *Appl. Surf. Sci.*, 2021, **542**, 148724.

38 M. Jahdi, S. B. Mishra, E. N. Nxumalo, S. D. Mhlanga and A. K. Mishra, Smart pathways for the photocatalytic degradation of sulfamethoxazole drug using F-Pd co-doped TiO_2 nanocomposites, *Appl. Catal., B*, 2020, **267**, 118716.

39 M. C. Ariza-Tarazona, J. F. Villarreal-Chiu and J. M. Hernández-López, *et al.*, Microplastic pollution reduction by a carbon and nitrogen-doped TiO_2: Effect of pH and temperature in the photocatalytic degradation process, *J. Hazard. Mater.*, 2020, **395**, 122632.

40 Q. Gao, F. Si, S. Zhang, Y. Fang, X. Chen and S. Yang, Hydrogenated F-doped TiO_2 for photocatalytic hydrogen evolution and pollutant degradation, *Int. J. Hydrogen Energy*, 2019, **44**(16), 8011–8019.

41 P. Niu, G. Wu, P. Chen, H. Zheng, Q. Cao and H. Jiang, Optimization of boron doped TiO_2 as an efficient visible light-driven photocatalyst for organic dye degradation with high reusability, *Front. Chem.*, 2020, **8**, 172.

42 A. Mancuso, O. Sacco and V. Vaiano, *et al.*, Visible light active Fe-Pr co-doped TiO_2 for water pollutants degradation, *Catal. Today*, 2021, **380**, 93–104, DOI: **10.1016/j.cattod.2021.04.018**.

43 X. Zhang, W. F. Chen and G. Bahmanrokh, *et al.*, Synthesis of V-and Mo-doped/codoped TiO_2 powders for photocatalytic degradation of methylene blue, *Nano-Struct. Nano-Objects*, 2020, **24**, 100557.

44 K. Bhuvaneswari, R. D. Bharathi and T. Pazhanivel, Silk fibroin linked Zn/Cd-doped SnO_2 nanoparticles to purify the organically polluted water, *Mater. Res. Express*, 2018, **5**(2), 24004.

45 L. Y. Yang, S. Y. Dong, J. H. Sun, J. L. Feng, Q. H. Wu and S. P. Sun, Microwave-assisted preparation, characterization and photocatalytic properties of a dumbbell-shaped ZnO photocatalyst, *J. Hazard. Mater.*, 2010, **179**(1–3), 438–443.

46 L. Radev, L. Pavlova and B. Samuneva, *et al.*, Sol–gel synthesis and structure of La_2O_3-CoO-SiO_2 powders, *Process. Appl. Ceram.*, 2008, **2**(2), 103–108.

47 S. P. Kim, M. Y. Choi and H. C. Choi, Photocatalytic activity of SnO_2 nanoparticles in methylene blue degradation, *Mater. Res. Bull.*, 2016, **74**, 85–89.

48 M. Said, P. L. Hariani and I. Apriani, in Solution combustion method to synthesize magnetic Fe_3O_4 as photocatalytic of Congo red dye and antibacterial activity, *IOP Conference Series: Earth and Environmental Science*, IOP Publishing, 2021, vol. 926, p. 12050.

49 P. Chhillar and P. B. Doon, Facile synthesis and photophysical properties of combustion derived Dy^{3+} doped $Ca_9La(PO_4)_7$ nanophosphors for advanced solid-state lighting applications, *Inorg. Chem. Commun.*, 2024, **159**, 111844, DOI: **10.1016/j.inoche.2023.111844**.

50 V. K. Gupta, R. Jain and A. Mittal, *et al.*, Photo-catalytic degradation of toxic dye amaranth on TiO_2/UV in aqueous suspensions, *Mater. Sci. Eng., C*, 2012, **32**(1), 12–17.

51 A. K. Gupta, A. Pal and C. Sahoo, Photocatalytic degradation of a mixture of Crystal Violet (Basic Violet 3) and Methyl Red dye in aqueous suspensions using Ag^+ doped TiO_2, *Dyes Pigm.*, 2006, **69**(3), 224–232.

52 S. Ameen, M. S. Akhtar, M. Nazim and H. S. Shin, Rapid photocatalytic degradation of crystal violet dye over ZnO flower nanomaterials, *Mater. Lett.*, 2013, **96**, 228–232.

53 H. Tian, J. Ma, K. Li and J. Li, Photocatalytic degradation of methyl orange with W-doped TiO_2 synthesized by a hydrothermal method, *Mater. Chem. Phys.*, 2008, **112**(1), 47–51.

54 J. Zhu, Y. Zhu, Y. Zhou, C. Wu, Z. Chen and G. Chen, Synergistic Promotion of Photocatalytic Degradation of Methyl Orange by Fluorine-and Silicon-Doped TiO_2/AC Composite Material, *Molecules*, 2023, **28**(13), 5170.

55 S. Lotfi, M. El Ouardi and H. A. Ahsaine, *et al.*, Low-temperature synthesis, characterization and photocatalytic properties of lanthanum vanadate $LaVO_4$, *Heliyon*, 2023, **9**(6), e17255.

56 G. M. Meselhy, M. Y. Nassar, I. M. Nassar and S. H. Seda, Auto-combustion synthesis of lanthanum-doped TiO_2 nanostructures for efficient photocatalytic degradation of crystal violet dye, *Mater. Res. Innov.*, 2024, 1–9.

57 B. D. Stojanovic, A. S. Dzunuzovic and N. I. Ilic, Review of methods for the preparation of magnetic metal oxides, *Magn., Ferroelectr., Multiferroic Met. Oxides*, 2018, 333–359, DOI: **10.1016/B978-0-12-811180-2.00017-7**.

58 B. Niu, F. Zhang and H. Ping, *et al.*, Sol–gel Autocombustion Synthesis of Nanocrystalline High-entropy Alloys, *Sci. Rep.*, 2017, **7**(1), 3421, DOI: **10.1038/s41598-017-03644-6**.

59 M. Y. Nassar, T. Y. Mohamed, I. S. Ahmed and I. Samir, MgO nanostructure via a sol–gel combustion synthesis method using different fuels: An efficient nano-adsorbent for the removal of some anionic textile dyes, *J. Mol. Liq.*, 2017, **225**, 730–740, DOI: **10.1016/j.molliq.2016.10.135**.

60 S. Naraginti, Y. Li, Y. Wu, C. Zhang and A. R. Upreti, Mechanistic study of visible light driven photocatalytic degradation of EDC 17α-ethinyl estradiol and azo dye Acid Black-52: phytotoxicity assessment of intermediates, *RSC Adv.*, 2016, **6**(90), 87246–87257.

61 Y. Fu, H. Chen, X. Sun and X. Wang, Combination of cobalt ferrite and graphene: High-performance and recyclable visible-light photocatalysis, *Appl. Catal., B*, 2012, **111–112**, 280–287, DOI: **10.1016/j.apcatb.2011.10.009**.

62 R. Hazime, C. Ferronato, L. Fine, A. Salvador, F. Jaber and J. M. Chovelon, Photocatalytic degradation of imazalil in an aqueous suspension of TiO_2 and influence of alcohols on the degradation, *Appl. Catal., B*, 2012, **126**, 90–99, DOI: **10.1016/j.apcatb.2012.07.007**.

63 D. A. H. Hanaor and C. C. Sorrell, Review of the anatase to rutile phase transformation, *J. Mater. Sci.*, 2011, **46**(4), 855–874, DOI: **10.1007/s10853-010-5113-0**.

64 W. Guan, F. Ji, Z. Xie, R. Li and N. Mei, Preparation and photocatalytic performance of nano-TiO_2 codoped with iron III and lanthanum III, *J. Nanomater.*, 2015, **2015**, 4.

65 A. Mancuso, N. Blangetti and O. Sacco, *et al.*, Photocatalytic Degradation of Crystal Violet Dye under Visible Light by Fe-

Doped TiO_2 Prepared by Reverse-Micelle Sol–Gel Method, *Nanomaterials*, 2023, **13**(2), DOI: 10.3390/nano13020270.

66 A. N. El-Shazly, G. S. El-Sayyad and A. H. Hegazy, *et al.*, Superior visible light antimicrobial performance of facet engineered cobalt doped TiO_2 mesocrystals in pathogenic bacterium and fungi, *Sci. Rep.*, 2021, **11**(1), 1–14, DOI: 10.1038/s41598-021-84989-x.

67 D. A. Solís-Casados, L. Escobar-Alarcón, L. M. Gómez-Oliván, E. Haro-Poniatowski and T. Klimova, Photodegradation of pharmaceutical drugs using Sn-modified TiO_2 powders under visible light irradiation, *Fuel*, 2017, **198**, 3–10.

68 A. K. Tripathi, M. C. Mathpal, P. Kumar, M. K. Singh, M. A. G. Soler and A. Agarwal, Structural, optical and photoconductivity of Sn and Mn doped TiO_2 nanoparticles, *J. Alloys Compd.*, 2015, **622**, 37–47.

69 J. Liqiang, S. Xiaojun, X. Baifu, W. Baiqi, C. Weimin and F. Honggang, The preparation and characterization of La doped TiO_2 nanoparticles and their photocatalytic activity, *J. Solid State Chem.*, 2004, **177**(10), 3375–3382.

70 M. Umair, D. Kim and M. Choi, Impact of climate, rising atmospheric carbon dioxide, and other environmental factors on water-use efficiency at multiple land cover types, *Sci. Rep.*, 2020, **10**(1), 1–13.

71 J. Zhu, J. Zhang, F. Chen, K. Iino and M. Anpo, High activity TiO_2 photocatalysts prepared by a modified sol–gel method: characterization and their photocatalytic activity for the degradation of XRG and X-GL, *Top. Catal.*, 2005, **35**, 261–268.

72 M. M. Mahlambi, A. K. Mishra, S. B. Mishra, R. W. Krause, B. B. Mamba and A. M. Raichur, Comparison of rhodamine B degradation under UV irradiation by two phases of titania nanophotocatalyst, *J. Therm. Anal. Calorim.*, 2012, **110**(2), 847–855.

73 X. Lin, J. Xing, W. Wang, Z. Shan, F. Xu and F. Huang, Photocatalytic activities of heterojunction semiconductors $Bi_2O_3/BaTiO_3$: a strategy for the design of efficient combined photocatalysts, *J. Phys. Chem. C*, 2007, **111**(49), 18288–18293.

74 S. M. Y. Qattali, J. Nasir and C. Pritzel, *et al.*, Synthesis and Characterization of Iron-Doped TiO_2 Nanotubes (Fe/TiNTs) with Photocatalytic Activity, *Constr. Mater.*, 2024, 315–328.

75 A. Mancuso, O. Sacco and V. Vaiano, *et al.*, Visible Light-Driven Photocatalytic Activity and Kinetics of Fe-Doped TiO_2 Prepared by a Three-Block Copolymer Templating Approach, *Materials*, 2021, **14**(11), DOI: 10.3390/ma14113105.

76 L. T. Jule, F. B. Dejene and A. G. Ali, *et al.*, Wide visible emission and narrowing band gap in Cd-doped ZnO nanopowders synthesized via sol–gel route, *J. Alloys Compd.*, 2016, **687**, 920–926, DOI: 10.1016/j.jallcom.2016.06.176.

77 S. Kader, M. R. Al-Mamun, M. B. K. Suhan, S. B. Shuchi and M. S. Islam, Enhanced photodegradation of methyl orange dye under UV irradiation using MoO_3 and Ag doped TiO_2 photocatalysts, *Environ. Technol. Innov.*, 2022, **27**, 102476, DOI: 10.1016/j.eti.2022.102476.

78 M. Zheng, H. Zhang and X. Gong, *et al.*, A simple additive-free approach for the synthesis of uniform manganese monoxide nanorods with large specific surface area, *Nanoscale Res. Lett.*, 2013, **8**, 1–7.

79 F. Davar, H. Hadadzadeh and T. S. Alaedini, Single-phase hematite nanoparticles: Non-alkoxide sol–gel based preparation, modification and characterization, *Ceram. Int.*, 2016, **42**(16), 19336–19342, DOI: 10.1016/j.ceramint.2016.09.104.

80 K. K. Pawar, L. S. Chaudhary and S. S. Mali, *et al.*, In_2O_3 nanocapsules for rapid photodegradation of crystal violet dye under sunlight, *J. Colloid Interface Sci.*, 2020, **561**, 287–297.

81 C. Sahoo, A. K. Gupta and A. Pal, Photocatalytic degradation of Crystal Violet (CI Basic Violet 3) on silver ion doped TiO_2, *Dye Pigm.*, 2005, **66**(3), 189–196.

82 M. Saeed, K. Albalawi and I. Khan, *et al.*, Synthesis of p–n NiO–ZnO heterojunction for photodegradation of crystal violet dye, *Alexandria Eng. J.*, 2023, **65**, 561–574, DOI: 10.1016/j.aej.2022.09.048.

83 H. Bayahia, High activity of $ZnFe_2O_4$ nanoparticles for photodegradation of crystal violet dye solution in the presence of sunlight, *J. Taibah. Univ. Sci.*, 2022, **16**(1), 988–1004, DOI: 10.1080/16583655.2022.2134696.

84 D. Gholami, S. Shahbazi and S. Mosleh, *et al.*, In situ growth of $CuFeS_2$/CuS bridged heterojunction catalyst with mixed redox-couple cations for excellent photocatalytic degradation of organophosphate insecticide: CFD and DFT modeling, *Chem. Eng. J.*, 2023, **461**, 141950, DOI: 10.1016/j.cej.2023.141950.

85 Y. Chen, X. Deng, J. Wen, J. Zhu and Z. Bian, Piezo-promoted the generation of reactive oxygen species and the photodegradation of organic pollutants, *Appl. Catal., B*, 2019, **258**, 118024, DOI: 10.1016/j.apcatb.2019.118024.

86 N. T. Nandhini, S. Rajeshkumar and S. Mythili, The possible mechanism of eco-friendly synthesized nanoparticles on hazardous dyes degradation, *Biocatal. Agric. Biotechnol.*, 2019, **19**, 101138, DOI: 10.1016/j.bcab.2019.101138.